

Research



Cite this article: Leng J, Xu H, Schaezner M, Pham MQ, Bourgeois G, Shanian A, Pasini D. 2021 Generalized tessellations of superelliptical voids in low porosity architected materials for stress mitigation. *Proc. R. Soc. A* **477**: 20200864. <https://doi.org/10.1098/rspa.2020.0864>

Received: 3 November 2020

Accepted: 18 January 2021

Subject Areas:

materials science, mechanical engineering, mechanics

Keywords:

architected material, stress concentration, low porosity, planar tessellation, void shape, superellipse

Author for correspondence:

Damiano Pasini

e-mail: damiano.pasini@mcgill.ca

Electronic supplementary material is available online at <https://doi.org/10.6084/m9.figshare.c.5300928>.

Generalized tessellations of superelliptical voids in low porosity architected materials for stress mitigation

Jiazhen Leng¹, Hang Xu¹, Megan Schaezner²,
Minh Quan Pham², Genevieve Bourgeois²,
Ali Shanian² and Damiano Pasini¹

¹Department of Mechanical Engineering, McGill University, 817 Sherbrooke Street West, Montreal QC H3A 0C3, Canada

²Siemens Power and Gas, 9545 Côte-de-Liesse, Dorval, QC H9P 1A5, Canada

JL, 0000-0002-9390-8426; MQP, 0000-0002-4744-435X; PD, 0000-0002-3021-7118

Stress concentration is a crucial source of mechanical failure in structural elements, especially those embedding voids. This paper examines periodic porous materials with porosity lower than 5%. We investigate their stress distribution under planar multiaxial loading, and presents a family of geometrically optimized void shapes for stress mitigation. We adopt a generalized description for both void geometry and planar tessellation patterns that can handle single and multiple voids of arbitrary void shape at a generic angle. The role of void shape evolution from diamond to rectellipse on the stress-distribution is captured at the edge of voids in a representative volume element (RVE) made of non-equal length periodic vectors. Theoretical derivations, numerical simulations along with experimental validation of the strain field in thermoplastic polymer samples fabricated by laser cutting unveil the role of geometric parameters, e.g. superellipse order, aspect ratio and rotation angle, that minimize stress peak and ameliorate stress distribution around voids. This work extends and complements classical theory by providing fundamental insights into the role that tessellation, void shape and inclination play in the stress distribution of low-porosity architected materials, thus introducing essential guidelines of broad application for stress-minimization and failure mitigation in diverse sectors.

1. Introduction

Architected materials can achieve exotic properties, potentially enabling a wider range of application across disciplines than conventional bulk materials [1–3]. Typically, it is the architecture of the building block rather than the chemical make-up that is designed by rationalized intuition [4] or shape [5] and topology optimization for designated functions [6–8]. Representative applications through the lens of mechanics of materials include maximum stiffness for structural integrity [9,10], enhanced fatigue life [11,12], maximum energy absorption and dissipation [13–15], negative modulus and mass density [16,17], or vanishing shear modulus [18,19]. The employment of tunable properties is also pervasive in other domains, such as auxeticity [20,21], wave propagation and acoustic band gaps [22–25], shape morphing and re-configuration [26–30], heat transfer [31,32], negative or zero coefficient of thermal expansion [33–35], biomedical devices [36–38], and many others [39].

Despite the abundance of research in porous architected materials, the majority focuses on high-porosity domains, preferably over 70% for greater tunability. Low porosity applications, i.e. below 5%, however, also exist, and are often employed in extreme environments subjected to severe service conditions [40–45]. Recent work on low-porosity metamaterials has shown the achievement of high tunability in both Poisson's ratio and band gaps through the use of staggered elliptical voids in orthogonal tessellations of ultralow porosity (less than 2%) [41,45]. Other works focused on non-elliptical slots with 'S' shape, and reported enhanced fatigue life [40], more broadband absorption for high-frequency acoustic noise [42], and improved cooling effectiveness than traditional circular voids [44]. Shifted and rotated straight slots in orthogonal tessellations have been also used in auxetic metamaterials with low-frequency band gaps [46,47]. On this front, most investigations focus on harnessing the well-studied mechanism of rotating units, where slots or cuts are introduced mainly in the form of circular shapes within orthogonal tessellations to generate auxetic responses.

Introducing slots in a design domain typically create sharp peaks of stress, a crucial source of mechanical failure in solids as well as in architected materials [48–50]. Classical works on stress concentration in solids examined mostly the impact of circular voids and other similar geometries in an infinite or semi-infinite domain mainly under uniform tension and other simple loading cases, some with consideration of reinforcements and anisotropic materials. Specific to cellular architectures, stress concentration has also been studied, but so far to a less degree. Most focused on high porosity metamaterials, hence investigating the relation between stress concentration and geometric imperfections induced by additive manufacturing [51,52]. On the low-porosity front, on the other hand, stress concentration, along with other aspects, such as crack nucleation, has been studied mainly in orthogonally tessellated metamaterials [43,53,54]. Several aspects remain so far unaddressed despite playing a key role on the impact of stress concentration in architected materials; these include (i) the stress field generated by voids with generic shape and the effect of boundary conditions on the edge of voids; (ii) the existence of optimal shape, beyond circular voids, and void interaction in a representative volume element (RVE); (iii) the role of generic tessellation patterns, beyond those defined by the normality of periodic vectors.

This paper on low-porosity metamaterials has a threefold objective: (i) examine voids with generic shapes and study the stress concentration field on their edges; (ii) identify optimized void geometries for minimum stress; (iii) understand the role of generic tessellation patterns with varying angle of periodic vectors and adjustable edge to length ratio under a general condition of biaxial loading. Section 2 introduces first a theoretical analysis supported by numeric simulations of stress distribution on the edge of generic voids in arbitrary planar tessellations, and then presents optimized parameters of void shapes for the mitigation of stress concentration. Section 3 presents the set-up of digital image correlation testing and in §4, the results of the strain fields are experimentally verified by the measurements of laser cut samples. Section 5, which precedes the conclusions, discusses the effect of tessellation pattern and loading conditions on the optimized system that minimizes peak stress on the edges of multiple voids.

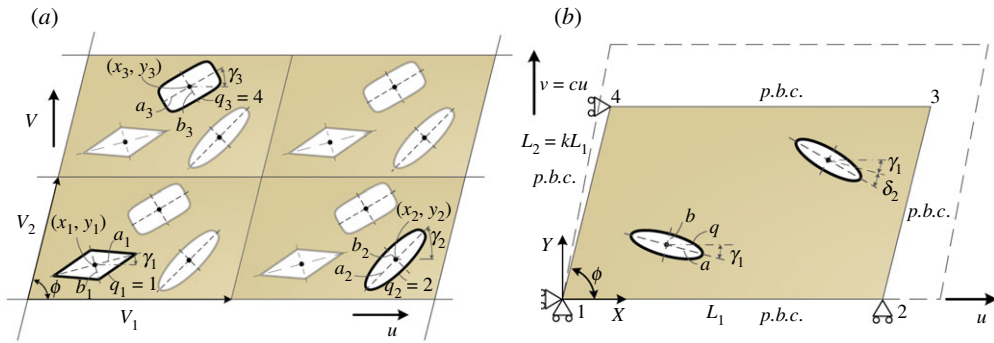


Figure 1. Definition of geometric parameters for tessellated superelliptical voids of low porosity in a planar domain. (a) Description of superelliptical voids and RVE; (b) RVE subject to displacement loading and periodic boundary conditions. Sketches of voids magnified for visualization purposes. RVE defined by periodic vectors, L_2 and L_1 , forming tessellation angle ϕ . γ defines void rotation from axis x . (Online version in colour.)

2. Stress concentration on the edge of a superelliptical void in representative volume element with low porosity

(a) Stress and strain fields in the representative volume element

We examine a two-dimensional architected material described by a generic RVE shaped with a parallelogram with varying angle between the periodic vectors, hence capable of describing arbitrary tessellations. Within the RVE we consider individual or multiple voids capturing a total area below 5%, each traceable by a generic shape that can range from asteroids, diamonds, to ellipses and rectellipses. Figure 1a shows representative shapes and number of voids in a two by two RVE describing a periodic domain.

For the description of void shape, we resort to Lamé curves describing a family of superelliptical curves. This formulation enables to outline the shape boundary of a generic void in the RVE through the manipulation of three parameters only, i.e. superellipse order, q , and ratio of semi-axis length, a and b , in a succinct form as

$$\left|\frac{x}{a}\right|^q + \left|\frac{y}{b}\right|^q = 1. \quad (2.1)$$

The main shape descriptors in the equation above are used in figure 1a to generate representative void shapes in a parallelogram RVE. For $q=2$, we retrieve the special case of elliptical voids. For varying q , other shapes emerge, such as asteroids ($q=2/3$), diamonds ($q=1$) and rectellipses ($q=4$). By varying q , the continuity of curvature changes, a factor that plays a key role in the stress-distribution on the edge of a void [48–50].

As per the tessellation pattern, our parallelogram RVE is defined by two periodic vectors, L_2 and L_1 , which can form a tessellation angle of ϕ , hence enabling a generic description of repetitive patterns beyond orthogonal (figure 1a). Within the RVE, the location of the void i is determined by the coordinates of its centre (x_i, y_i) and its rotation angle γ_i from the horizontal axis (figure 1a). Their relative rotation, δ_i is also defined to describe the existence of multiple voids within the RVE (figure 1b), a notion here presented to describe different tessellation patterns, such as hexagonal and Kagome, as illustrated in a later section of the paper.

The area of the void is determined from the porosity is ψ

$$\psi = n \frac{A_{\text{void}}}{A_{\text{RVE}}}, \quad (2.2)$$

where we assume that multiple voids ($n > 1$) in the RVE are of given area. For a prescribed area of the void, A_{void} , the aspect ratio a/b of the superellipse can be used as another independent

parameter besides the order q and the semi-axis lengths to write A_{void} as a function of the gamma function

$$A_{\text{void}} = 4ab \frac{(\Gamma(1 + 1/q))^2}{\Gamma(1 + 2/q)}. \quad (2.3)$$

The equations above describing void geometry and tessellation pattern are used in the following to derive the stress and strain fields in the RVE under the following assumptions:

- (i) The material domain is unbounded, periodic and subjected to uniform displacement in the X and Y directions of the global Cartesian system. Stress and strain analysis of the planar tessellation is thus inferred from the study of the RVE under periodic boundary conditions.
- (ii) The porosity is considered to be lower than 5%, thereby enabling the adoption of the bulk material properties of the solid for the RVE. This assumption infers that the interaction of multiple voids in the RVE is practically negligible.
- (iii) The RVE undergoes small deformation and the material behaviour is linear elastic, thus small strain theory applies to the theoretical derivation.

Figure 1b shows the parallelogram RVE subjected to a generic biaxial displacement u and v with $v = cu$. Varying c allows to retrieve uniaxial loading conditions as $c = -\mu \sin(\phi)$, where μ is Poisson's ratio. By aligning the horizontal edge of the RVE to the global X axis, we can write the periodic boundary conditions on its edges as

$$\begin{aligned} u_R - u_L &= u_2 - u_1, v_R - v_L = v_2 - v_1 && \text{for left and right} \\ u_T - u_B &= u_4 - u_1, v_T - v_B = v_4 - v_1 && \text{for top and bottom} \end{aligned} \quad (2.4)$$

where the subscripts mark the right (R), left (L), top (T) and bottom (B) edges and four vertices of the RVE in figure 1b.

To suppress rigid body motion and to model the general case of the existence of shear strain in the RVE, we apply a set of four homogeneous boundary conditions at node 1, 2 and 4 (figure 1b). This choice is necessary to capture non-zero shear strains in an RVE tessellated at an angle other than 90° . By contrast, constraining only three degrees of freedom would fail to capture non-zero shear strains.

$$\left. \begin{aligned} u_1 &= v_1 = 0 \\ v_2 &= 0 \\ u_4 &= 0. \end{aligned} \right\} \quad (2.5)$$

The strain field in the solid RVE can then be derived for $\phi \neq 0$. The combination of equation (2.4) and (2.5) allows the existence of non-zero shear strain in the RVE for ϕ other than 90°

$$\left. \begin{aligned} \epsilon_{xx} &= \frac{\partial u}{\partial x} = \frac{u}{L_1} \\ \epsilon_{yy} &= \frac{\partial v}{\partial y} = c \frac{u}{kL_1 \sin(\phi)} \\ \gamma_{xy} &= \frac{\partial u}{\partial y} + \frac{\partial v}{\partial x} = -\frac{u}{L_1} \cot(\phi). \end{aligned} \right\} \quad (2.6)$$

Solving the eigenvalue problem of the matrix form of equation (2.6) with $\epsilon_{xy} = \gamma_{xy}/2$ yields the principal strain for $0^\circ < \phi \leq 90^\circ$ as

$$\left. \begin{aligned} \epsilon_1 &= \frac{u \left(c + k \sin(\phi) - \sqrt{c^2 - 2kc \sin(\phi) + k^2} \right)}{2kL_1 \sin(\phi)} \\ \epsilon_2 &= \frac{u \left(c + k \sin(\phi) + \sqrt{c^2 - 2kc \sin(\phi) + k^2} \right)}{2kL_1 \sin(\phi)} \end{aligned} \right\} \quad (2.7)$$

The corresponding principal directions can thus be determined as the inverse tangent of the eigenvectors

$$\left. \begin{aligned} v_1 &= \left[\frac{c - k \sin(\phi) + \sqrt{c^2 - 2kc \sin(\phi) + k^2}}{k \cos(\phi)}, 1 \right] \\ v_2 &= \left[\frac{c - k \sin(\phi) - \sqrt{c^2 - 2kc \sin(\phi) + k^2}}{k \cos(\phi)}, 1 \right] \end{aligned} \right\} \quad (2.8)$$

The assumptions (i) to (iii) also enable us to adopt the plane stress conditions. Multiplying the constitutive matrix of the linear elastic material with the principal strains in equation (2.7) yields two principal stresses

$$\left. \begin{aligned} \sigma_1 &= - \frac{Eu \left[(1 + \mu)(c + k \sin(\phi)) - (1 - \mu)\sqrt{c^2 - 2kc \sin(\phi) + k^2} \right]}{2kL_1 \sin(\phi) (\mu^2 - 1)} \\ \sigma_2 &= - \frac{Eu \left[(1 + \mu)(c + k \sin(\phi)) + (1 - \mu)\sqrt{c^2 - 2kc \sin(\phi) + k^2} \right]}{2kL_1 \sin(\phi) (\mu^2 - 1)} \end{aligned} \right\} \quad (2.9)$$

where E and μ are Young's modulus and Poisson's ratio of the bulk material.

If we consider the case of uniaxial displacement loading, in the horizontal direction (u), the vertical displacement can be obtained from u by setting c as $-\mu \sin(\phi)$. Inserting this expression into equations (2.7) to (2.9) yields

$$\left. \begin{aligned} \sigma_1 &= \frac{u \left(k - \mu - \sqrt{k^2 \cot^2(\phi) + \mu^2 + 2k\mu + k^2} \right)}{2kL_1} \\ \sigma_2 &= \frac{u \left(k - \mu + \sqrt{k^2 \cot^2(\phi) + \mu^2 + 2k\mu + k^2} \right)}{2kL_1} \end{aligned} \right\} \quad (2.10)$$

$$\left. \begin{aligned} v_1 &= \left[- \frac{k + \mu - \sqrt{k^2 \cot^2(\phi) + \mu^2 + 2k\mu + k^2}}{k \cot(\phi)}, 1 \right] \\ v_2 &= \left[- \frac{k + \mu + \sqrt{k^2 \cot^2(\phi) + \mu^2 + 2k\mu + k^2}}{k \cot(\phi)}, 1 \right] \end{aligned} \right\} \quad (2.11)$$

$$\left. \begin{aligned} \sigma_1 &= \frac{Eu(\mu - k)}{2kL_1(\mu - 1)} - \frac{Eu\sqrt{\mu^2 + 2k\mu + k^2}/\sin^2(\phi)}{2kL_1(\mu + 1)} \\ \sigma_2 &= \frac{Eu(\mu - k)}{2kL_1(\mu - 1)} + \frac{Eu\sqrt{\mu^2 + 2k\mu + k^2}/\sin^2(\phi)}{2kL_1(\mu + 1)} \end{aligned} \right\} \quad (2.12)$$

The rhombus-shaped RVE is a special case obtained by setting $k = 1$ in the equations above.

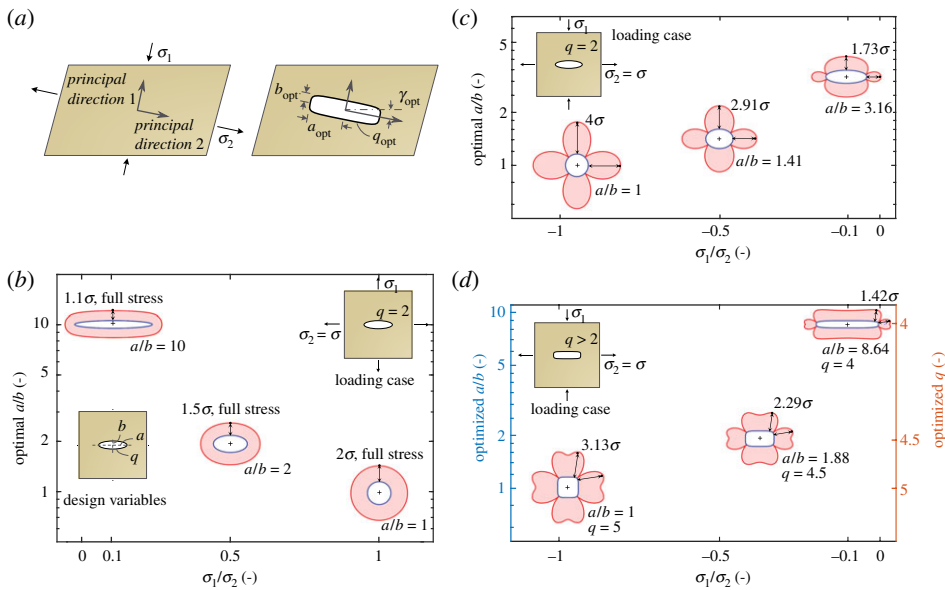


Figure 2. Shapes and stress distribution of optimal elliptical and optimized superelliptical voids for peak stress minimization. (a) Principal directions and the optimized axis alignment for a superelliptical void. Optimal elliptical voids and their stress distribution for (b) $0 < \sigma_1/\sigma_2 \leq 1$, and (c) $-1 \leq \sigma_1/\sigma_2 < 0$. Optimized superelliptical voids and their stress distribution for (d) $-1 \leq \sigma_1/\sigma_2 < 0$. (Online version in colour.)

(b) Optimized shape of low porosity superelliptical void for mitigation of peak stress

In this section, we first examine the special case of an elliptical void ($q = 2$) and find in closed form its optimum shape, i.e. the optimum aspect ratio, and then study numerically the generic scenario of the optimum shape of a void with $q \neq 2$.

(i) Optimized elliptical holes

Equation (2.9) provides the two principal stresses in the RVE, where the void—either elliptical or superelliptical—is embedded with directions given by equation (2.8). An exemplary RVE under biaxial loading is shown on the left of figure 2a.

The low porosity assumption enables us to treat the void within an RVE as loaded by σ_1 and σ_2 in an infinitely large domain. Theoretical derivation verified numerically (see the electronic supplementary material S1) have shown the optimal rotation γ for the mitigation of stress concentration makes the longer semi-axis of the elliptical void aligned with the principal direction of the larger principal stress, as shown in the right plot of figure 2a. Further results in the next subsection show this alignment applies to superelliptical voids too.

Under the condition of void alignment with the principal axes, we can now find the optimal a/b of the elliptical void in closed-form, while the optimized q , and a/b for a superelliptical void are found numerically in the next sections. For elliptical voids, we consider the stress concentration factor of an arbitrary rotated void within the RVE as

$$K_t = \frac{\sigma_{\max}}{\sigma_2}, \quad (2.13)$$

where σ_{\max} is the largest von Mises stress on the edge of the void and σ_2 is the larger principal stresses in magnitude, taken as the reference stress herein.

The theoretical formulae of the optimal elliptical void aspect ratio that minimizes K_t and the minimum value of K_t (see details of derivation in electronic supplementary material, S1) are given

by

$$\text{optimal } \frac{a}{b} = \begin{cases} \frac{1}{\sigma_1/\sigma_2} & \text{for } 0 < \frac{\sigma_1}{\sigma_2} \leq 1 \\ \frac{1}{\sqrt{-\sigma_1/\sigma_2}} & \text{for } -1 \leq \frac{\sigma_1}{\sigma_2} < 0 \end{cases} \quad (2.14)$$

and

$$\min K_t = \begin{cases} 1 + \sigma_1/\sigma_2 & \text{for } 0 < \frac{\sigma_1}{\sigma_2} \leq 1 \\ \left(1 + \sqrt{-\left(\frac{\sigma_1}{\sigma_2}\right)}\right)^2 & \text{for } -1 \leq \frac{\sigma_1}{\sigma_2} < 0. \end{cases} \quad (2.15)$$

Equations (2.14) and (2.15) are used to generate six plots of stress distributions collected in figure 2*b,c* for optimal elliptical voids for the following bi-axial loading cases: $\sigma_1/\sigma_2 = \pm 1, \pm 0.5$ and ± 0.1 . From the results, it emerges

- (i) For $\sigma_1/\sigma_2 > 0$ (figure 2*b*), the optimal elliptical void can achieve full stress state on the edge. As per equations (2.14) and (2.15), the optimal a/b is the reciprocal of σ_1/σ_2 and the minimum K_t is a linear function of σ_1/σ_2 . The optimal a/b decreases to 1 and the minimum K_t increases to 2 as σ_1/σ_2 approaches 1.
- (ii) For $\sigma_1/\sigma_2 < 0$ (figure 2*c*), the maximum stress is attained at the four tips. The results show that for given magnitude of σ_1/σ_2 , the optimal a/b is larger for $-1 < \sigma_1/\sigma_2 < 0$ than for $0 < \sigma_1/\sigma_2 < 1$ because for the former the square root appears in equation (2.14). The minimum K_t is larger for $\sigma_1/\sigma_2 < 0$, and the largest difference is 100% for $\sigma_1/\sigma_2 = -1$ when compared with $\sigma_1/\sigma_2 = 1$.
- (iii) If $\sigma_1/\sigma_2 = 0$, the optimal parameters are the limit of equation (2.14) and (2.15) with $a/b = \infty$ and $K_t = 1$. This implies that approaching the uniaxial principal stress makes the optimal elliptical hole evolve into an infinitely thin slit aligned with the loading direction, and the maximum von Mises stress on the tip of the crack to converge to the value of the loading stress.

(ii) Optimized superelliptical holes

For superelliptical void with $q \neq 2$, no closed-form solution of the stress field exists on the edge of a void in an infinite domain. In this section, we first numerically solve the problem for given geometric parameters, and then optimize the void geometry to find the parameters that minimize K_t .

A square RVE with $\phi = 90^\circ$ and $\psi = 0.25\%$ is modelled using ABAQUS (SIMULIA, Providence, RI). The boundary conditions given by equation (2.4) and (2.5) are implemented. Young's modulus and Poisson's ratio of the base material are $E = 7.0 \times 10^4$ MPa and $\mu = 0.35$. After a convergence test, approximately 15000 quadratic plane stress elements with local mesh refinement and curvature control are employed. Further details of the finite-element simulation are available in the supplementary material S2. The superellipse order q falls in the set of (1.5, 2, 3, 4, 5, 6) and the aspect ratio a/b varies in the set of (1, 2, 4, 10, 20). The rotation angle γ ranges between -90° and 90° by an increment of 10° . By tuning the ratio c between biaxial displacement loadings, a series of principal stress ratio can be obtained (see equation (2.9)). A numerical optimization implemented in Matlab (MathWorks, Natick, MA) on the best result of the parametric study follows to identify the optimized parameters of the superelliptical void that minimize stress concentration. The results are plotted in figure 2*d* plots for the following loading cases: $\sigma_1/\sigma_2 = -1, -0.5$ and -0.1 . A number of insights can be drawn from the results and from a relative comparison of the plots in figure 2*c,d*

- (i) First, the numerical results confirm that the void axis alignment with the principal directions obtained in the previous section in closed form also holds for general superelliptical voids.

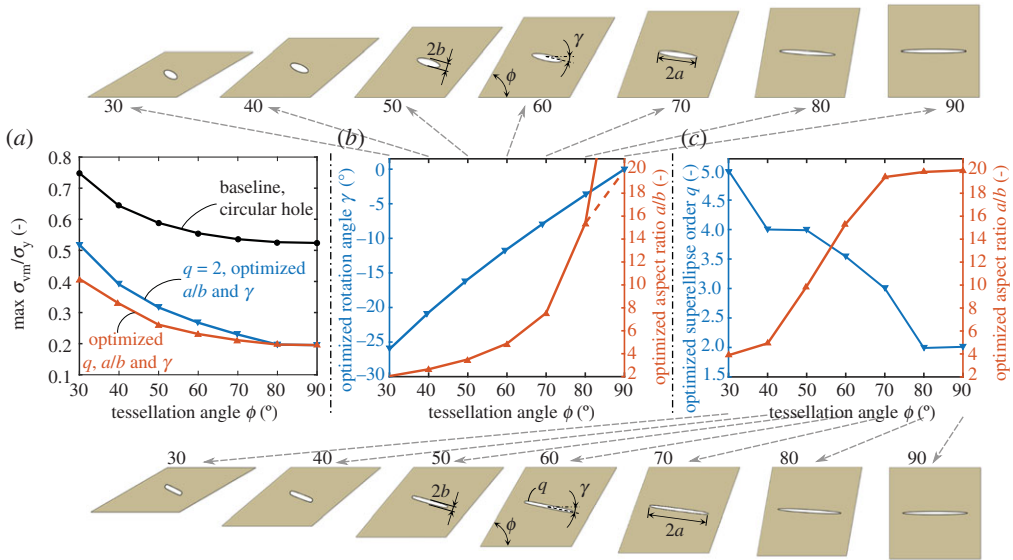


Figure 3. Optimized geometries of superelliptical voids for rhombus RVE under uniaxial displacement. (a) Normalized min values of peak von Mises stress versus tessellation angle for elliptical and superelliptical voids; (b) Rotation angle and aspect ratio of optimized elliptical voids; (c) Superellipse order and aspect ratio of optimized superelliptical voids. Sketches of voids magnified for visualization purposes. (Online version in colour.)

- (ii) Superelliptical voids with $q > 2$ can further reduce the stress concentration factor by 18% to 22% from elliptical voids when $\sigma_1/\sigma_2 < 0$.
- (iii) Superelliptical voids with $q > 2$ features a continuous change of curvature at their edge reaching a maximum at their corners and zero at their tips. Given the tight relation between stress concentration and curvature, the ideal full-stress distribution can be better approximated by a distribution of stress that achieves the full-stress at eight points on the edge, two around each corner, as opposed to four points only for elliptical voids.
- (iv) As σ_1/σ_2 reduces from 0 to -1 , the optimized a/b reduces and converges to 1 while the optimized q increases up to 5.
- (v) For $-1 < \sigma_1/\sigma_2 < 0$, the optimized a/b of the superelliptical void is always larger than the elliptical counterpart.

(iii) Optimized superellipse in rhombus-shaped representative volume element

To exemplify the application of the above findings to low porosity architected materials with RVE tessellated in a planar domain, we now study the effect of the tessellation angle γ , and for given values of γ we find the optimized geometry of the void including superellipse order q and ratio of semi-axis length a/b . We examine a generic superelliptical void at the centre of a rhombus-shaped RVE, with porosity $\psi = 0.25\%$, periodic vectors of equal length, $k=1$ (figure 1b), and under uniaxial displacement loading u . The architected material is made out of a representative metal with yield stress $\sigma_y = 275$ MPa.

To study the role of tessellation angle, we assume to vary it discretely of 10° between the representative values 30° and 90° , and consider the resulting seven scenarios for the cases of $q=2$ and $q > 2$, all satisfying the boundary conditions in equations (2.4) and (2.5). We emphasize that for $\phi \neq 90^\circ$ the principal stresses are biaxial (see equation (2.12)), and the ratio of σ_1/σ_2 in the RVE increases from -0.239 at $\phi = 30^\circ$ to 0 at $\phi = 90^\circ$.

Figures 3 illustrates three related plots all emphasizing the role of ϕ on the x -axis. The first (figure 3a) shows the peak von Mises stress, here normalized by the yield stress of the representative metal, for the optimized elliptical and superelliptical void as well as for the

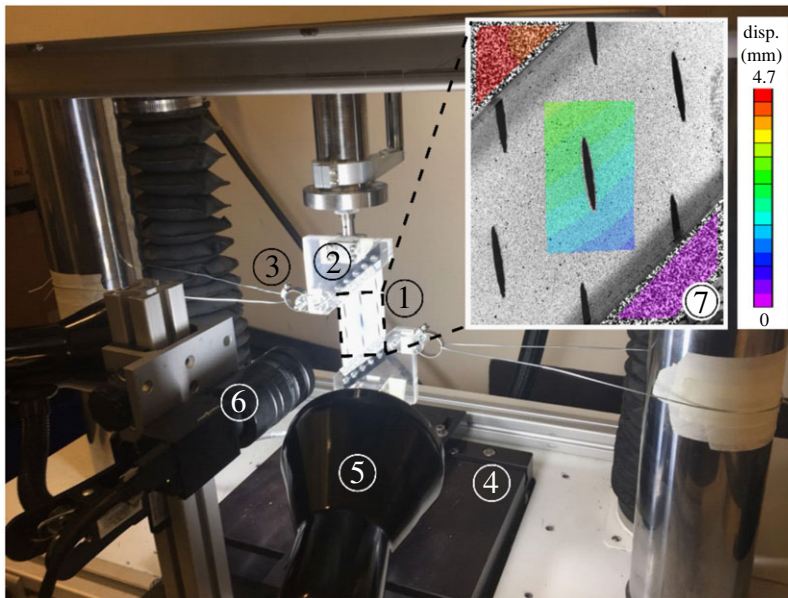


Figure 4. Experimental set-up used to measure strain fields of low porosity architected materials. ① Test sample; ② Fixture; ③ Horizontal connection tab and steel wire; ④ TA ElectroForce 3510 Test Instrument; ⑤ Write Light; ⑥ CCD camera and ⑦ Displacement fields of fixtures and test sample (unit in mm). (Online version in colour.)

reference circular void, each reported for given ϕ . The second and the third (figure 3*b,c*), illustrated their corresponding optimized parameters, i.e. rotation angle, aspect ratio and superellipse order.

From a comparison of the results in figure 3*a*, we observe that the decrease of the peak stress achieved by the superelliptical family is outstanding: an optimized elliptical void can achieve at least 31.8% of decrease of peak stress (at $\phi = 30^\circ$) from its circular counterpart, and an optimized superelliptical void can even reach 45.4% decrease at $\phi = 30^\circ$. Furthermore, the effect of the optimized superelliptical order for $q > 2$ is more significant for a smaller ϕ , as the value of σ_1/σ_2 is even lower than zero, and the optimized $q = 2$ when $\sigma_1/\sigma_2 = 0$. As per the void rotation, the values of the optimized a/b in figure 3*b* match exactly the theoretical value of equation (2.11) and demonstrate the alignment of the void with the principal directions. With regard to the ratio of the void axes, the optimized a/b in figure 3*b* increases with the decrease of ϕ and the values are in agreement with the predictions obtained by using equation (2.14) for $-1 \leq \sigma_1/\sigma_2 < 0$.

For superelliptical voids with $q > 2$, the optimized values of γ for each ϕ are identical to those of the elliptical voids, hence only the set of the latter are displayed in figure 3*c*. Here, the evolution of the optimized q and a/b shows that for σ_1/σ_2 even smaller than zero, i.e. for decreasing ϕ , the optimized q gets even larger than 2, and can be up to 5; by contrast, the optimized a/b decreases with a decrease of ϕ . A comparison between figure 3*b,c* manifests that the a/b of optimized superelliptical void is always larger than that of the optimized elliptical baseline, but the difference tends to vanish as ϕ increases to 90° . For $\sigma_1/\sigma_2 = 0$ at $\phi = 90^\circ$, the optimized a/b is 20, reaching the upper bound set in the approximation of infinity for the numerical solution.

3. Fabrication and test procedure

(a) Description of sample fabrication and mechanical testing

To validate the research findings both from theory and computation, a digital image correlation system of a charge-coupling device camera and the DIC correlation software Vic-2D (Correlate Solution Inc.) was used to measure the strain field of eleven representative samples. Their

geometry is shaped into a parallelogram of tessellation angle ϕ with length of 90 mm and width of 50 mm. All test samples were made of 0.318 mm thick glycol modified polyethylene terephthalate (PETG) and were laser cut by TROTEC Laser GmbH (Austria). A 3 by 3 pattern of voids of 2% porosity was set at the central portion of the sample. Prior to testing, the samples were coated in white paint and then a fine pattern of black paint was added by an air sprayer for contrast.

(b) Mechanical testing

Each sample was first subject to a pre-tension of 50 N and then loaded to 300 N. The preloading was applied to remove initial gaps and tighten the tester grips to the sample. The configuration of the sample under a given loading was selected as the reference for the DIC measurement capturing the deformation from 50 N to 300 N.

For parallelogram samples with $\phi \neq 90^\circ$, the boundary conditions in equations (2.4) and (2.5) are demanding to implement in a real setting. For this reason, we designed a special rig of trapezoidal fixtures and horizontal connection tabs (figure 4) to provide transverse fixation on the lateral sides of the sample. While the rig allows to accommodate the biaxial principal stress field of equation (2.12) for samples with $\phi \neq 90^\circ$, in our testing it was sufficient to apply only a uniaxial load at the end of the sample. For a detailed description of the test set-up, see electronic supplementary material, S3.

4. Validation results and comparison with numerical simulations

The tests were separated into four groups. Group I examines the effect of the aspect ratio. Group II addresses the effect of rotation of voids to illustrate the importance of the alignment with the principal direction. Group III investigates the impact of superellipse order on the strain pattern. Group IV focuses on the relative rotation between two voids in the RVE and its influence on the peak strain. The raw data from DIC were the displacement and strain fields of the sample. The principal strain around the centre void was selected as the metric for comparison of simulation versus test results.

The samples of Group I were fabricated with the following parameters $\phi = 90^\circ$, $q = 2$, $a/b = 1$ and 4, 10. For $\phi = 90^\circ$, the loading creates a uniaxial principal stress in the sample and the alignment to the principal direction is obtained by laying the long semi-axis of elliptical voids along the loading direction. Additional set of finite-element models (ABAQUS; SIMULIA, Providence, RI) of the as-built sample with three-dimensional geometry were created and meshed by quadratic brick elements with local refinement. The material response was assumed as linear elastic with $E = 4200$ MPa and $\mu = 0.4$ available from the manufacturer of the raw material. Additional details on this set of finite-element models for as-built samples are reported in electronic supplementary material, S2.

Figure 5a,b shows the results of test measurements along with a comparison between simulations and test results for Group I under uniaxial displacement loading on an RVE with $\phi = 90^\circ$. Presented in the contour plot figure 5a, the numerical results confirm that aligning elliptical holes with the principal directions is the best choice for the mitigation of stress concentration. In addition, the three sample configurations marked in the contour plot (figure 5a), each with its own sketch on the top, were fabricated and tested. Their numerical and testing results are shown in figure 5b. The comparison of the strain distribution on the edge of the centre void between them demonstrates a very good match for all three samples. The peak strain is always observed at the tips of the short semi-axis and the pattern is symmetrical. Both the experimental and simulation results confirm the trend, we obtain from the theory in the loading case of uniaxial stress: the peak principal strain reduces as a/b increases. Quantitatively, the simulation results are uniformly higher than the tests by no more than 30%. This can be attributed to the accuracy of the test set-up: DIC cannot measure a small margin on the edge of the void as observed in all samples, and the strain/stress field decays away from the edge [50], resulting in a smaller measured value. The width of the margin differs among samples and cannot be accurately estimated, and the rate

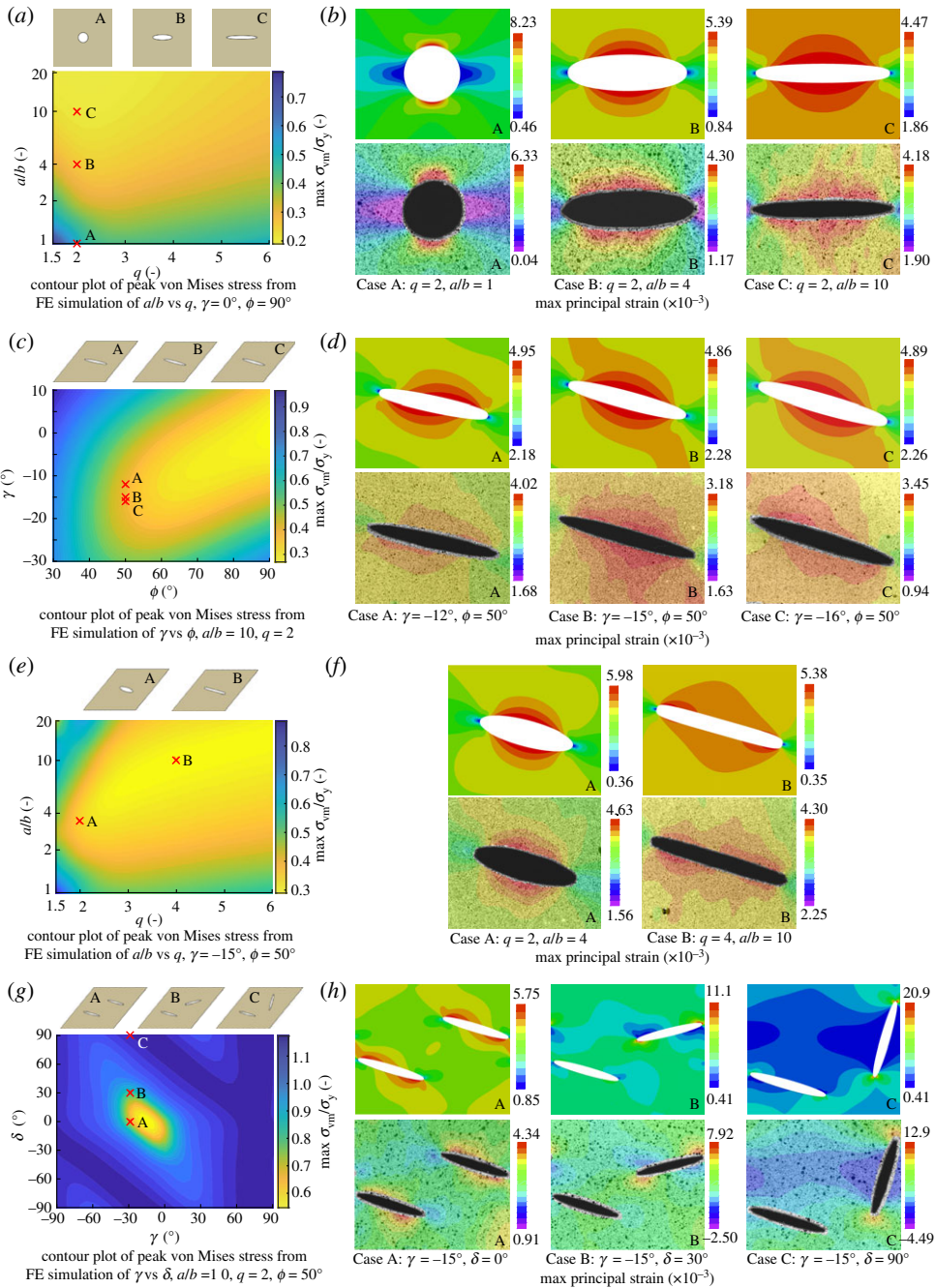


Figure 5. Contour plots of FE simulation results and comparison with test results showing the effect of a/b , q , γ and δ , test samples are marked by the symbol 'x' in red. (a) Contour plot of peak von Mises stress from FE simulation of a/b versus q , $\gamma = 0^\circ$, $\phi = 90^\circ$. (b) Group I: variation of a/b , $q = 2$, $\gamma = 0^\circ$, $\phi = 90^\circ$. (c) Contour plot of peak von Mises stress from FE simulation of γ versus ϕ , $a/b = 10$, $q = 2$, $\phi = 50^\circ$. (d) Group II: variation of γ , $a/b = 10$, $q = 2$, $\phi = 50^\circ$. (e) Contour plot of peak von Mises stress from FE simulation of a/b versus q , $\gamma = -15^\circ$, $\phi = 50^\circ$. (f) Group III: variation of q and a/b , $\gamma = -15^\circ$, $\phi = 50^\circ$. (g) Contour plot of peak von Mises stress from FE simulation of γ versus δ , $a/b = 10$, $q = 2$, $\phi = 50^\circ$. (h) Group IV: variation of δ , $a/b = 10$, $q = 2$, $\gamma = -15^\circ$, $\phi = 50^\circ$. (Online version in colour.)

of strain/stress decay is dependent on the shape of the void, thereby explaining the difference in percentage errors. The accuracy of DIC is also sensitive to spot size and spot density on the sample and the specifications of the hardware, yet these play a minor role in this work.

Group II consists of three samples with $\phi = 50^\circ$, $q = 2$ and $a/b = 10$. The angle of rotation varies among them such as $\gamma = -12^\circ$, -15° and -16° respectively. The actual tests were performed by incrementing γ by 1° until the identification of the optimized value that corresponded to the minimum principal strain; therefore the three cases presented herein are representative. The ridge of the optimized γ that minimizes the peak stress for each ϕ in the contour plot of figure 5c corresponds to the principal direction predicted by equation (2.11). Figure 5d shows a good match of the strain pattern for each case. The optimized rotation angle is $\gamma = -15^\circ$, an angle at which the location of the peak strain is symmetric about the long axis of the elliptical void. Any deviation from it, even by 1° , causes a shift in the peak strain, thereby spoiling symmetry and generating an increase of the peak strain value. The theoretical prediction of the optimized γ is -15.9° by equation (2.8), which only differs by 0.9° . The tests and simulations of Group II verify the alignment of the void with the principal direction for stress/strain minimization and support the validity of the closed form expression derived for the principal direction. The $\sim 30\%$ error observed from the DIC measurement, which may underestimate the magnitude of the peak strain, still exists, and the reasons can be attributed to those discussed above for Group I.

Group III is the direct comparison of a set of optimized void shapes for $\phi = 50^\circ$. More specifically optimized elliptical voids with $q = 2$, $a/b = 4$ (figure 3b) versus optimized superelliptical voids with $q = 4$, $a/b = 10$ (figure 3c). Figure 5e shows the contour plot of representative geometries with varying a/b , q for given $\phi = 50^\circ$. As per the value of γ , we note that the samples were manufactured with $\gamma = -15^\circ$, the value of void rotation found from the results of Group II, as opposed to -15.9° which is the theoretically obtained value. From the comparison of the strain patterns in figure 5f, we evince the superiority of superelliptical voids. The test results suggest that the superelliptical void (right) can achieve 7.2% lower peak strain than the elliptical counterpart (left), while the simulations indicate that the decrease can be 10%. Both tests and simulations manifest that the superelliptical void can reach the peak strain at locations near its four corners (although not perfectly symmetric due to the imperfect implementation of boundary conditions). On the other hand, for the elliptical void the peak strain can localize at the tips of the short axis only. The test measurements are approximately 20% smaller than the simulation results. In summary, also for this group of tests the DIC measurements verify our arguments on the optimized orientation, superellipse order and aspect ratio for the minimization of stress concentration.

Group IV further investigates the effect of multiple voids in one RVE. Assuming all voids are congruent and sufficiently spaced from each other to minimize mutual interaction at low porosity, the only variable that pertains is δ , the relative rotation between two voids in the RVE (figure 1a). To study the effect of δ , we fabricate samples with $\phi = 50^\circ$ for three representative geometries sharing the parameters $q = 2$, $a/b = 10$, $\gamma = -15^\circ$, and differing for $\delta = 0^\circ$, 30° and 90° . These are marked in the contour plot of figure 5g. The results in figure 5h shows that the peak strain is sensitive to the relative rotation of voids; it nearly doubles when δ increases from 0° to 30° and further enlarges at $\delta = 90^\circ$. To minimize the peak strain, multiple low-porosity voids should be identical with respect to translation. Also here we observe a very good qualitative match of the strain patterns. The quantitative error increases as δ deviates from 0° and approaches 90° . Finally, we note that the experimental results of this last group of tests are also representative of other types of tessellation, e.g. hexagonal patterns, as explained in the next section.

5. Beyond single void representative volume element: the role of tessellations in low porosity architected materials

The research findings above for the minimization of peak stress on the edge of superelliptical voids in planar RVE can be ideally extended to address arbitrary planar tessellations. Varying

Table 1. Summary of parameters and reduction of peak von Mises stress of void shapes for tessellations with $\phi = 60^\circ$ and $\nu = 0.25\%$ in figure 6.

load case	optimized void	reference void	no. of voids in the RVE	difference of σ_{vmMax}
$u \neq 0, v = 0$	$q = 3.5$	$q = 2$	1	−59%
	$a/b = 15.4$	$a/b = 1$	2	−59%
	$\gamma = -11.7^\circ$	$\gamma = 0$	3	−59%
$u \neq 0, v = 0.43u$	$q = 2$	$q = 2$	1	−33%
	$a/b = 1.65$	$a/b = 1$	2	−33%
	$\gamma = -24.6^\circ$	$\gamma = 0$	3	−33%

the tessellation angle ϕ , the edge length ratio k and the number of voids in the RVE n enables to represent a large set of tessellations. For example, for $\phi = 60^\circ$ we can retrieve a family of classical and widely applied tessellations including triangular, hexagonal and Kagome tessellations. What is specific to each of them, however, is n , the number of voids in the RVE, respectively one, two and three, as shown in the RVEs indicated in blue in figure 6.

We now focus on a representative tessellation defined by $\phi = 60^\circ$ and discuss the role of n in the RVE. The relative positions of the centres of voids in the RVE are determined by the geometry of the tessellation; here we assume that multiple voids in the RVE have identical geometry except for their relative rotations (figure 6). We study the effect of void number through numerical analysis and optimization along with validation experiments for RVE of 0.25% porosity under two load cases: (i) uniaxial horizontal displacement and (ii) biaxial tension, defined by $v = 0.43u$.

The optimized voids for each tessellation under each load case are juxtaposed in figure 6. Figure 6*a–d* pertain to the uniaxial displacement load case, while the others, (figure 6*e–h*) correspond to the load case of biaxial displacement. The circular void in the triangular tessellation is here selected as the reference. The key observation from all cases in the figure 6 is that for the minimization of peak stress in low-porosity planar architected materials, the result is not sensitive to the number of voids in the RVE. This is due to the small value of porosity, ruling out void interaction. For the mitigation of stress concentration, the triangular, hexagonal and Kagome tessellations all need to respect the optimized values of q , a/b and γ found in §2, despite their difference of n from 1 to 3; their values of peak stress are also equal.

For the uniaxial displacement loading case, $\sigma_1/\sigma_2 = -0.042$, and the optimized shape approaches a long and narrow superelliptical void (figure 5*b–d*). In addition, the values of their γ matches the predictions obtained from equation (2.8). The accompanying colour bar visualizes the peak von Mises stress normalized by the yield stress. By comparing the results in figure 6, we observe the following. The optimized void shape yields a 59% decrease of the peak stress from that of the reference circular void.

For the biaxial tension case, $\sigma_1/\sigma_2 = 0.605$, and the optimized shape is an elliptical void, as this can reach the full-stress distribution everywhere on the edge. Also for this case, the optimized γ equals the theoretical prediction, and the decrease of the peak stress is 33%. To summarize the results of the two examples, the parameters of the optimized and reference voids along with the reduction of peak von Mises stress are provided in table 1. Examples herein together with those in figure 3 demonstrate that the adoption of optimized shapes for super-elliptical voids in low-porosity planar tessellations can significantly decrease the amount of stress concentration to values below those yielded by traditional circular voids.

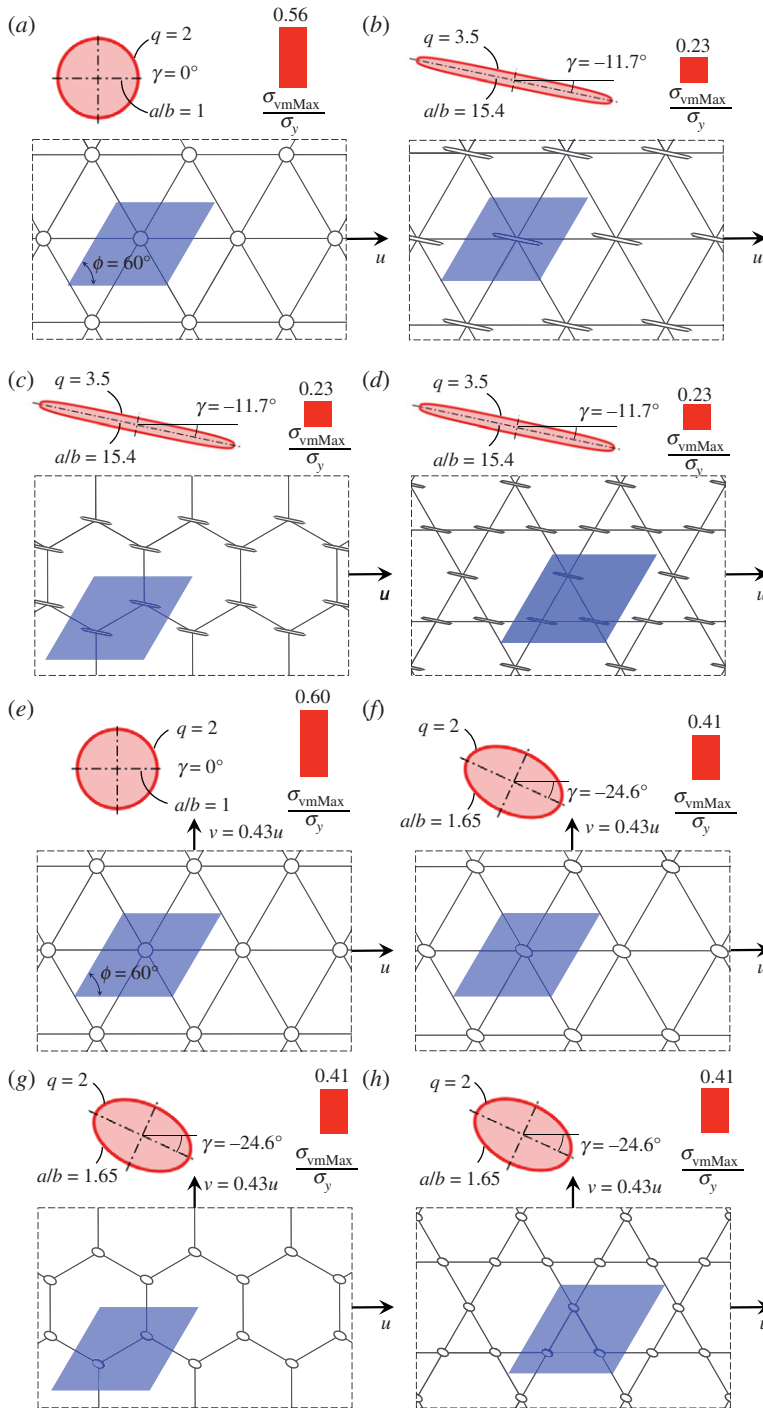


Figure 6. Comparison of peak stress between tessellations in the family of $\phi = 60^\circ$. (a) Triangular tessellation, circular voids under uniaxial displacement. (b) Triangular tessellation, optimized superelliptical voids under uniaxial displacement. (c) Hexagonal tessellation, optimized superelliptical voids under uniaxial displacement. (d) Kagome tessellation, optimized superelliptical voids under uniaxial displacement. (e) Triangular tessellation, circular voids under biaxial displacement. (f) Triangular tessellation, optimized superelliptical voids under biaxial displacement. (g) Hexagonal tessellation, optimized superelliptical voids under biaxial displacement. (h) Kagome tessellation, optimized superelliptical voids under biaxial displacement. (Online version in colour.)

Table 2. Summary of optimized parameters of a (super)elliptical void and K_t for the range of loading conditions: $-1 \leq \sigma_1/\sigma_2 \leq 1$.

σ_1/σ_2	elliptical void		σ_1/σ_2	elliptical void		Superelliptical void		
	a/b	K_t		a/b	K_t	q	a/b	K_t
1.0	1.00	2.00	−1.0	1.00	4.00	5.0	1.00	3.13
0.9	1.11	1.90	−0.9	1.05	3.80	5.0	1.10	3.01
0.8	1.25	1.80	−0.8	1.12	3.59	5.0	1.27	2.85
0.7	1.43	1.70	−0.7	1.20	3.37	5.0	1.40	2.66
0.6	1.67	1.60	−0.6	1.29	3.15	5.0	1.62	2.47
0.5	2.00	1.50	−0.5	1.41	2.91	4.5	1.88	2.29
0.4	2.50	1.40	−0.4	1.58	2.66	4.5	2.36	2.12
0.3	3.33	1.30	−0.3	1.83	2.40	4.5	3.08	1.90
0.2	5.00	1.20	−0.2	2.23	2.09	4.5	4.55	1.69
0.1	10.0	1.10	−0.1	3.16	1.73	4.0	8.64	1.42

The findings presented in this paper can be generalized in compact form to provide guidelines of broad application for low-porosity architected materials with planar tessellation. The following are procedural steps for the minimization of stress concentration, here categorized with respect to the number of voids present in the RVE.

(a) Tessellations with single void in the RVE

- (i) Determine the principal directions and the principal stresses by using equation (2.8) and (2.9) with the properties of the solid material and the RVE.
- (ii) Align the long axis of the void with the principal direction of the larger principal stresses in magnitude. Failing to do so can result in a large increase of peak stress, even when the deviation from this optimal condition is small. For example, the worst-case scenario of our investigation shows that by perturbing of only one degree the optimized elliptical hole with $a/b = 20$ and $\phi = 90^\circ$, we can incur in a 5.4% increase of stress. The increase goes up to 126% for a mere 5 degree deviation.
- (iii) Select the optimized geometric parameters of the (super)elliptical voids for given loading conditions, as tabulated in compact form in table 2. For $q = 2$ (elliptical voids), the values are determined using equation (2.14) and (2.15). For $q > 2$ (superelliptical voids), the optimized parameters are determined numerically. The results show that for $\sigma_1/\sigma_2 > 0$, the optimal elliptical void renders a full-stress state; if $\sigma_1/\sigma_2 < 0$ the optimized superelliptical voids can approximate the full-stress state better than the elliptical ones. The additional decrease of peak von Mises stress can be 18% to 22% as σ_1/σ_2 approaches -1 . The optimized a/b of superelliptical void for $\sigma_1/\sigma_2 < 0$ is close (difference $< 12\%$) to the optimized a/b of the elliptical void for $\sigma_1/\sigma_2 > 0$ with the identical absolute value. Furthermore, as σ_1/σ_2 decreases to -1 , the order of the optimized q for the superelliptical void increases to 5.

(b) Tessellations with multiple voids in the representative volume element

- (i) For very low porosity, e.g. below 5%, the interaction between voids in the RVE can be neglected (figure 6). For this reason, the results presented above in point (iii) still hold for

generic tessellations defined by other than normal periodic vectors as long as the multiple voids containing in the RVE share the same geometry.

The results gained from this study are valuable for the design of low porosity architected material with minimum level of stress. Our work extends the classical theory of stress concentration by considering periodic boundary conditions and biaxial displacement loading. It contributes to gain practical insights into the effect of arbitrary planar tessellations, and provides optimized parameters of (super)elliptical voids that can achieve or approximate the full stress state, a condition that in turn smooths out stress concentration. Further questions can be addressed to refine the current outcomes. First, it is necessary to estimate a precise upper bound of porosity for the validity of the independent action of voids. While the minimum distance between neighbouring voids for their interaction to be considered inconsequential, cannot be prescribed precisely for a general problem, relevant guidelines can be found in the literature [50]. Second, for the case of $\sigma_1/\sigma_2 < 0$, superelliptical voids outperform elliptical ones as they can better approximate the full-stress state, but the existence of other void shapes that may perform even better is still to explore. Shape and topology optimization can be a powerful numerical tool for this purpose. Other than current assumptions of linear elastic materials and small strains, the work can be extended to account for finite deformation, damage, plasticity and other more complex physical phenomena.

6. Conclusion

This paper has examined generic planar tessellations of superelliptical voids in a low-porosity domain under biaxial displacement loading. Theoretical derivations and numerical simulations have identified the optimized geometric parameters of superelliptical voids for the mitigation of stress concentration. Upon the alignment with the principal direction corresponding to the largest principal stress, optimized superelliptical voids can more significantly reduce the peak stress than circular voids by achieving full-stress at multiple locations on the edge of the void. DIC tests validate the results with satisfactory level of agreement. The findings presented herein augment the classical theory of stress concentration by delivering important principles on the role of void shape and inclination, as well as tessellation, in the stress distribution of low-porosity architected materials. Finally, general guidelines have been proposed for the mitigation of failure with recommendations that are suitable for a broad range of engineering applications.

Ethics. This research was designed and performed without any involvement of human or animal products or any interference of participants personal data. Hence, the authors hereby claim no ethical implications.

Data accessibility. The data related to theoretical derivations are available within the article and its electronic supplementary material. Computational modelling data supporting the findings of this study are available from Mendeley Data repository [55]. <http://dx.doi.org/10.17632/ddkwcmbsb4w.1>.

Authors' contributions. D.P. and J.L. conceived the idea, research and methodology. J.L. performed the theoretical derivation and the finite-element analysis of RVE models. J.L. also selected the parameters of test samples and modelled the test samples for finite-element analysis. H.X. designed the test rig, made the CAD drawings and samples, performed the testing and helped modelling the test samples. D.P. discussed and supervised the understanding of the findings of this work. All authors contributed to the final manuscript.

Competing interests. The authors declare that they have no known competing financial interests or personal relationships that could have appeared to influence the work reported in this paper.

Funding. This work was funded by the Natural Sciences and Engineering Research Council of Canada and Siemens Canada (grant nos. 242363 and 242561).

Disclaimer. Any opinions, findings and conclusions or recommendations expressed in this publication are those of the authors and do not necessarily reflect the views of Siemens and NSERC.

References

1. Ashby M, Bréchet Y. 2003 Designing hybrid materials. *Acta Mater.* **51**, 5801–5821. (doi:10.1016/S1359-6454(03)00441-5)

2. Bertoldi K. 2017 Harnessing instabilities to design tunable architected cellular materials. *Annu. Rev. Mater. Res.* **47**, 51–61. (doi:10.1146/annurev-matsci-070616-123908)
3. Schaedler TA, Carter WB. 2016 Architected cellular materials. *Annu. Rev. Mater. Res.* **46**, 187–210. (doi:10.1146/annurev-matsci-070115-031624)
4. Overvelde JT, Weaver JC, Hoberman C, Bertoldi K. 2017 Rational design of reconfigurable prismatic architected materials. *Nature* **541**, 347–352. (doi:10.1038/nature20824)
5. Lehman J, Lakes R. 2013 Stiff lattices with zero thermal expansion and enhanced stiffness via rib cross section optimization. *Int. J. Mech. Mater. Des.* **9**, 213–225. (doi:10.1007/s10999-012-9210-x)
6. Ha S-H, Lee HY, Hemker KJ, Guest JK. 2019 Topology optimization of three-dimensional woven materials using a ground structure design variable representation. *J. Mech. Des.* **141**, 061403. (doi:10.1115/1.4042114)
7. Osanov M, Guest JK. 2016 Topology optimization for architected materials design. *Annu. Rev. Mater. Res.* **46**, 211–233. (doi:10.1146/annurev-matsci-070115-031826)
8. Pasini D, Guest JK. 2019 Imperfect architected materials: mechanics and topology optimization. *MRS Bull.* **44**, 766–772. (doi:10.1557/mrs.2019.231)
9. Chen W, Watts S, Jackson JA, Smith WL, Tortorelli DA, Spadaccini CM. 2019 Stiff isotropic lattices beyond the maxwell criterion. *Sci. Adv.* **5**, eaaw1937. (doi:10.1126/sciadv.aaw1937)
10. Han SC, Kang K. 2019 Another stretching-dominated micro-architected material, shellular. *Mater. Today* **31**, 31–38. (doi:10.1016/j.mattod.2019.05.018)
11. Abad EMK, Khanoki SA, Pasini D. 2013 Fatigue design of lattice materials via computational mechanics: application to lattices with smooth transitions in cell geometry. *Int. J. Fatigue* **47**, 126–136. (doi:10.1016/j.ijfatigue.2012.08.003)
12. Dallago M, Winiarski B, Zanini F, Carmignato S, Benedetti M. 2019 On the effect of geometrical imperfections and defects on the fatigue strength of cellular lattice structures additively manufactured via selective laser melting. *Int. J. Fatigue* **124**, 348–360. (doi:10.1016/j.ijfatigue.2019.03.019)
13. Chen X, Ji Q, Wei J, Tan H, Yu J, Zhang P, Laude V, Kadic M. 2020 Light-weight shell-lattice metamaterials for mechanical shock absorption. *Int. J. Mech. Sci.* **169**, 105288. (doi:10.1016/j.ijmecsci.2019.105288)
14. Haghpahan B, Shirazi A, Salari-Sharif L, Izard AG, Valdevit L. 2017 Elastic architected materials with extreme damping capacity. *Extreme Mech. Lett.* **17**, 56–61. (doi:10.1016/j.eml.2017.09.014)
15. Pham M-S, Liu C, Todd I, Lertthanasarn J. 2019 Damage-tolerant architected materials inspired by crystal microstructure. *Nature* **565**, 305–311. (doi:10.1038/s41586-018-0850-3)
16. Liu X-N, Hu G-K, Huang G-L, Sun C-T. 2011 An elastic metamaterial with simultaneously negative mass density and bulk modulus. *Appl. Phys. Lett.* **98**, 251907. (doi:10.1063/1.3597651)
17. Oh JH, Kwon YE, Lee HJ, Kim YY. 2016 Elastic metamaterials for independent realization of negativity in density and stiffness. *Sci. Rep.* **6**, 1–10. (doi:10.1038/s41598-016-0001-8)
18. Hedayati R, Leeflang A, Zadpoor A. 2017 Additively manufactured metallic pentamode metamaterials. *Appl. Phys. Lett.* **110**, 091905. (doi:10.1063/1.4977561)
19. Kadic M, Bückmann T, Stenger N, Thiel M, Wegener M. 2012 On the practicability of pentamode mechanical metamaterials. *Appl. Phys. Lett.* **110**, 191901. (doi:10.1063/1.4709436)
20. Gao Z, Liu D, Tománek D. 2018 Two-dimensional mechanical metamaterials with unusual Poisson ratio behavior. *Phys. Rev. Appl.* **10**, 064039. (doi:10.1103/PhysRevApplied.10.064039)
21. Grima-Cornish JN, Grima JN, Attard D. 2020 A novel mechanical metamaterial exhibiting auxetic behavior and negative compressibility. *Materials* **13**, 79. (doi:10.3390/ma13010079)
22. Chen Y, Li T, Scarpa F, Wang L. 2017 Lattice metamaterials with mechanically tunable Poisson's ratio for vibration control. *Phys. Rev. Appl.* **7**, 024012. (doi:10.1103/PhysRevApplied.7.024012)
23. Jafari H, Yazdi MRH, Fakhrabadi MMS. 2019 Wave propagation in microtubule-based bio-nano-architected networks: a lesson from nature. *Int. J. Mech. Sci.* **164**, 105175. (doi:10.1016/j.ijmecsci.2019.105175)
24. Li S, Zhao D, Niu H, Zhu X, Zang J. 2018 Observation of elastic topological states in soft materials. *Nat. Commun.* **9**, 1–9. (doi:10.1038/s41467-017-02088-w)
25. Rafsanjani A, Pasini D. 2016 Bistable auxetic mechanical metamaterials inspired by ancient geometric motifs. *Extreme Mech. Lett.* **9**, 291–296. (doi:10.1016/j.eml.2016.09.001)

26. Haghpahan B, Salari-Sharif L, Pourrajab P, Hopkins J, Valdevit L. 2016 Multistable shape-reconfigurable architected materials. *Adv. Mater.* **28**, 7915–7920. (doi:10.1002/adma.201601650)
27. Liu L, Qiao C, An H, Pasini D. 2019 Encoding kirigami bi-materials to morph on target in response to temperature. *Sci. Rep.* **9**, 1–14. (doi:10.1038/s41598-018-37186-2)
28. Rafsanjani A, Akbarzadeh A, Pasini D. 2015 Snapping mechanical metamaterials under tension. *Adv. Mater.* **27**, 5931–5935. (doi:10.1002/adma.201502809)
29. Rafsanjani A, Akbarzadeh A, Pasini D. 2017 Buckling-induced kirigami. *Phys. Rev. Lett.* **118**, 084301. (doi:10.1103/PhysRevLett.118.084301)
30. Taniker S, Celli P, Pasini D, Hofmann D, Daraio C. 2020 Temperature-induced shape morphing of bi-metallic structures. *Int. J. Solids Struct.* **190**, 22–32. (doi:10.1016/j.ijsolstr.2019.10.024)
31. Iasiello M, Bianco N, Chiu WK, Naso V. 2019 Thermal conduction in open-cell metal foams: anisotropy and representative volume element. *Int. J. Therm. Sci.* **137**, 399–409. (doi:10.1016/j.ijthermalsci.2018.12.002)
32. Yang H, Li Y, Yang Y, Chen D, Zhu Y. 2019 Effective thermal conductivity of high porosity open-cell metal foams. *Int. J. Heat Mass Transf.* **147**, 118974. (doi:10.1016/j.ijheatmasstransfer.2019.118974)
33. Parsons EM. 2019 Lightweight cellular metal composites with zero and tunable thermal expansion enabled by ultrasonic additive manufacturing: modeling, manufacturing, and testing. *Compos. Struct.* **223**, 110656. (doi:10.1016/j.compstruct.2019.02.031)
34. Xu H, Farag A, Pasini D. 2017 Multilevel hierarchy in bi-material lattices with high specific stiffness and unbounded thermal expansion. *Acta Mater.* **134**, 155–166. (doi:10.1016/j.actamat.2017.05.059)
35. Xu H, Farag A, Pasini D. 2018 Routes to program thermal expansion in three-dimensional lattice metamaterials built from tetrahedral building blocks. *J. Mech. Phys. Solids* **134**, 54–87. (doi:10.1016/j.jmps.2018.04.012)
36. Arabnejad S, Johnston B, Tanzer M, Pasini D. 2017 Fully porous 3d printed titanium femoral stem to reduce stress-shielding following total hip arthroplasty. *J. Orthop. Res.* **35**, 1774–1783. (doi:10.1002/jor.23445)
37. Rahimizadeh A, Nourmohammadi Z, Arabnejad S, Tanzer M, Pasini D. 2018 Porous architected biomaterial for a tibial-knee implant with minimum bone resorption and bone-implant interface micromotion. *J. Mech. Behav. Biomed. Mater.* **78**, 465–479. (doi:10.1016/j.jmbbm.2017.11.041)
38. Zadpoor AA. 2019 Mechanical performance of additively manufactured meta-biomaterials. *Acta Biomater.* **85**, 41–59. (doi:10.1016/j.actbio.2018.12.038)
39. Zadpoor AA. 2016 Mechanical meta-materials. *Mater. Horiz.* **3**, 371–381. (doi:10.1039/C6MH00065G)
40. Javid F *et al.* 2017 On the design of porous structures with enhanced fatigue life. *Extreme Mech. Lett.* **16**, 13–17. (doi:10.1016/j.eml.2017.08.002)
41. Javid F, Wang P, Shanian A, Bertoldi K. 2016 Architected materials with ultra-low porosity for vibration control. *Adv. Mater.* **28**, 5943–5948. (doi:10.1002/adma.201600052)
42. Jetté F-X, Shanian A, Schaezner M, Pham MQ, Bourgeois G, Farhangi M, Sanchez F, Innes M. 2017 Acoustic properties of perforated liners with perpendicular arrangements of narrow slots. In *Proc. Turbo Expo: Power for Land, Sea, and Air*, p. V04AT04A061. New York, NY: American Society of Mechanical Engineers.
43. Leng J, Reynolds G, Schaezner M, Pham MQ, Bourgeois G, Shanian A, Pasini D. 2018 Stress concentration in low-porosity periodic tessellations with generic patterns of elliptical holes under biaxial strain. *J. Appl. Mech.* **85**, 101010. (doi:10.1115/1.4040539)
44. Shanian A *et al.* 2019 Application of multifunctional mechanical metamaterials. *Adv. Eng. Mater.* **21**, 1900084. (doi:10.1002/adem.201900084)
45. Taylor M, Francesconi L, Gerendás M, Shanian A, Carson C, Bertoldi K. 2014 Low porosity metallic periodic structures with negative Poisson's ratio. *Adv. Mater.* **26**, 2365–2370. (doi:10.1002/adma.201304464)
46. Tian X, Chen W, Gao R, Liu S, Wang J. 2020 Design of pore layout for perforated auxetic metamaterials with low-frequency band gaps. *Appl. Phys. Express* **13**, 045503. (doi:10.35848/1882-0786/ab7f5b)

47. Tian X, Chen W, Gao R, Liu S, Wang J. 2020 Perforation-rotation based approach for band gap creation and enlargement in low porosity architected materials. *Compos. Struct.* **245**, 112331. (doi:10.1016/j.compstruct.2020.112331)
48. Inglis CE. 1913 Stresses in a plate due to the presence of cracks and sharp corners. *Trans. - Soc. Nav. Archit. Mar. Eng.* **55**, 193–198.
49. Neuber H. 1961 Theory of stress concentration for shear-strained prismatical bodies with arbitrary nonlinear stress-strain law. *J. Appl. Mech.* **28**, 544–550. (doi:10.1115/1.3641780)
50. Pilkey WD, Pilkey DF. 2008 *Peterson's stress concentration factors*. Hoboken, NJ: John Wiley & Sons.
51. Dallago M, Raghavendra S, Fontanari V, Benedetti M. 2020 Stress concentration factors for planar square cell lattices with filleted junctions. *Mater. Des. Process. Commun.* **2**, e98. (doi:10.1002/mdp2.98)
52. Lohmuller P, Favre J, Piotrowski B, Kenzari S, Laheurte P. 2018 Stress concentration and mechanical strength of cubic lattice architectures. *Materials* **11**, 1146. (doi:10.3390/ma11071146)
53. Francesconi L, Baldi A, Dominguez G, Taylor M. 2020 An investigation of the enhanced fatigue performance of low-porosity auxetic metamaterials. *Exp. Mech.* **60**, 93–107. (doi:10.1007/s11340-019-00539-7)
54. Francesconi L, Taylor M, Baldi A. 2019 An investigation of stress concentration, crack nucleation, and fatigue life of thin low porosity metallic auxetic structures. In *Fracture, fatigue, failure and damage evolution*, pp. 65–71, vol. 6. Lecture Notes in Physics. Cham, Switzerland: Springer International Publishing.
55. Pasini D. 2020 Data for paper on superelliptical voids in arbitrary tessellations. Mendeley Data, V1. (doi:10.17632/ddkwcmsb4w.1)